Optimizing radiation patterns of mechanically reconfigurable phased arrays using flexible meta-gaps

D. Elliott Williamstyer[1,2] (iD) and Ali Hajimiri[1]

[1]Department of Electrical Engineering, California Institute of Technology, Pasadena, CA, USA and [2]Department of Engineering, Hofstra University, Hempstead, NY, USA

CAMBRIDGE UNIVERSITY PRESS

Abstract

In order to take on arbitrary geometries, shape-changing arrays must introduce gaps between their elements. To enhance performance, this unused area can be filled with meta-material inspired switched passive networks on flexible sheets in order to compensate for the effects of increased spacing. These flexible meta-gaps can easily fold and deploy when the array changes shape. This work investigates the promise of meta-gaps through the measurement of a 5-by-5 λ-spaced array with 40 meta-gap sheets and 960 switches. The optimization and measurement problems associated with such a high-dimensional phased array are discussed. Simulated and *in-situ* optimization experiments are conducted to examine the differential performance of metaheuristic algorithms and characterize the underlying optimization problem. Measurement results demonstrate that in our implementation meta-gaps increase the average main beam power within the field of view (FoV) by 0.46 dB, suppress the average side lobe level within the FoV by 2 dB, and enhance the field-of-view by 23.5° compared to a ground-plane backed array.

Introduction

The recent development of mechanically shape-changing phased arrays shows the promise of using geometric reconfiguration to optimize for a given array behavior [1]. However, Gauss's *Theorema Egregium* requires that the surface area of an array must stretch or contract as it changes between shapes with different Gauss curvature [2]. If the number of radiators in an array is fixed, the spacing between them must change as the array shifts between planar and spherical shapes. Thus, arrays of rigid tiles can only change shape if *gaps* are introduced between the tiles or tiles are removed from the surface [3].

The required increased element spacing alters array performance by reducing the fill factor, introducing grating lobes, and changing the antenna coupling. But these gaps also present an opportunity in the form of extra unused area on the radiation surface that can be filled with switch-controlled flexible passive structures capable of distorting the near-field environment. Such meta-surface inspired structures, henceforth referred to as *meta-gaps*, can be used to mitigate the effects of increased element spacing.

Figure 1 illustrates the advantages of *flexible* meta-gaps. In a planar shape there are no gaps, so the meta-gaps fold behind ground-plane backed antennas where they will minimally interact with the radiating surface. When the array changes into a cylinder, the meta-gaps are deployed between the antennas and are configured to mitigate the effects of increased antenna spacing or otherwise enhance the array performance.

In-situ *meta-gap optimization concept*

Meta-gaps introduce parasitic metal structures in the gaps of an array in order to distort the near-field environment, thus altering the far-field behavior, antenna coupling, and port impedances. The challenge is identifying *which* metal patterns benefit the array performance. Unfortunately, electromagnetic fields are nonlinear with respect to their boundary conditions and so adding conductors can drastically change their fundamental behavior. The difficulty of this design problem is exacerbated in the context of a phased array because the near-field is subject to different field excitations, each of which will induce different currents on the conductor surfaces and therefore alter their impact of the array behavior. Thus the behavior of the structure must be considered under *every desired excitation*.

Inspired by the work of Lavaei and Babakhani [4], we present a switch-controlled meta-gap structure capable of dynamic reconfiguration. The structure consists of a grid of metal squares connected to each other by RF switches. These switches can be turned on and off to create conductive pathways that control how and where currents are excited. With a fine enough grid,
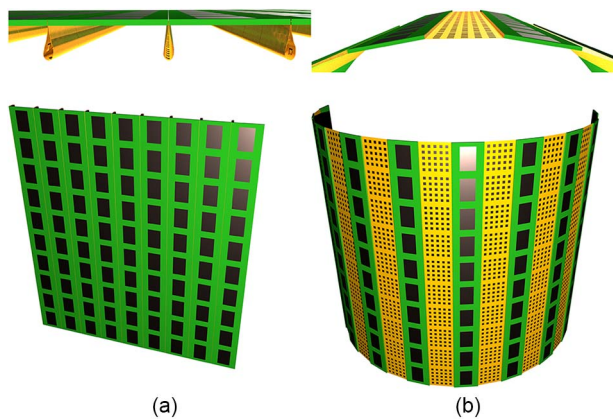
Figure 1. Illustration of how meta-gaps can be deployed to fill the gaps in a shape-changing array. (a) In planar configuration, the sheets fold behind the tiles. (b) In cylindrical configuration they expand to fill the gaps. Reprinted with permission from the copyright holder, EuMA.

the switches can essentially program the shape of conductors on the surface into an arbitrary configuration. This concept is similar to the pixel-based automated design of waveguide couplers presented in [5].

By using programmable switches, the meta-gap conductor patterns can be dynamically reconfigured *in-situ*, allowing optimization methods to be used on a physical array to explore a large number of candidate patterns to identify solutions that enhance array performance. This *in-situ* optimization avoids the accuracy and model complexity issues associated with simulating a large array, providing an excellent platform to explore meta-gap performance. *In-situ* optimization establishes a minimum bound of performance for optimal realized meta-gap structures and allows the nature of the design space and properties of optimal solutions to be inferred from the relative performance of different optimization algorithms.

Prior art

The use of switches and meta-materials to alter antenna and array performance is well explored. PIN diodes have been used to alter the operation frequency [6], polarization [7], and radiation patterns of both antennas and arrays [8, 9]. Techniques include using switches to reconfigure the conductor geometry [10, 11], alter resonator modes [12], change the array feed [13], or select different elements [14–16]. Switches have also been used to modify parasitic conductors and adjust the near-field environment [17, 18].

Embedding meta-materials in radiating structures is another well-traveled research avenue. Meta-materials have been used in arrays to reduce antenna coupling [19–21] and reduce the size of a linear array [22]. They have also been used in antenna designs to reduce the antenna size [23], increase its bandwidth [24], and alter its polarization [25]. Switch based meta-materials have been used to change the selectivity of a frequency-selective surface [26] and modify the radiation pattern of a dipole antenna [27].

Switched RF structures and meta-materials are useful for a broad range of applications. Switched parasitic structures can be used to modulate the radiation pattern to enable physically secure wireless communication [28]. Pattern reconfiguration enables blind optimization of transceiver patterns to mitigate interference and multi-path effects using a constant modulus algorithm [29].

Reconfigurable antennas are also useful for in-orbit satellite adaptation, enhanced MIMO systems, and cognitive radio techniques [30]. Surfaces of programmable meta-materials have enabled programmable reflector arrays [31, 32], passive relays [33], and holography at THz frequencies [34].

Outline

An earlier version of this paper was presented at the 2022 European Microwave Conference and was published in its Proceedings [35]. This paper expands on that work with additional experiments that relax the identical sheet restriction, simulated experiments to identify the statistical properties of the optimization algorithms, and more in-depth discussions, explanations, and analyses.

Section "Phased-Array Optimization" discusses the complexities of phased array characterization and the meta-gap optimization problem. Section "Simulated Statistical Analysis" presents statistical results of optimizations preformed on a simulated model. Section "Demonstration Array" describes the hardware and measurement approach used to perform *in-situ* optimization. Three rounds of *in-situ* optimization experiments are presented in '*In-Situ* Optimization Experiments' section. Finally section "Discussion" takes a holistic view of the experimental and simulated results before section "Conclusions" concludes.

Phased-array optimization

Completely characterizing the performance of a phased array requires numerous measurements. A full 3D radiation pattern must be measured for every beam angle within the steering range in order to get a *complete* picture of the power radiated in both the desired (main beam) and undesired (side lobe) directions. Managing this measurement complexity is critical for characterizing meta-gaps because each switch configuration effectively creates a new array that requires complete characterization.

Array figures of merit

In order to reduce the number of measurements used for characterization, we evaluate the performance of the array using three criteria: the power radiated in the main beam direction (MBP), the side lobe level (SLL), and the field of view (FoV) in the E- and H-plane cuts. SLL is here defined as the relative strength of the peak side lobe[1] with respect to the MBP and FoV is defined as the range over which the SLL is negative. These measures provide insight into the array's maximum effective isotropic radiated power (EIRP), 3-dB steering range, and gain, without requiring a full 3D scan.

In order to characterize the performance of the array with a single number for optimization purposes, the *average* MBP and SLL over the FoV, and the *average* FoV over the different ϕ cuts, are used as the optimization criteria as shown in Figure 2. Using an average ensures that the array performance is over its entire steering range and not just in one direction.

Beams are only steered within the FoV when characterizing the MBP and SLL because, due to spatial aliasing, the phase settings required to steer a beam outside of the FoV are the same as those that steer a beam at a different angle *inside* of the FoV. Since the

---

[1]Note that by this definition, grating lobes are considered side lobes and thus the SLL can be *positive*.
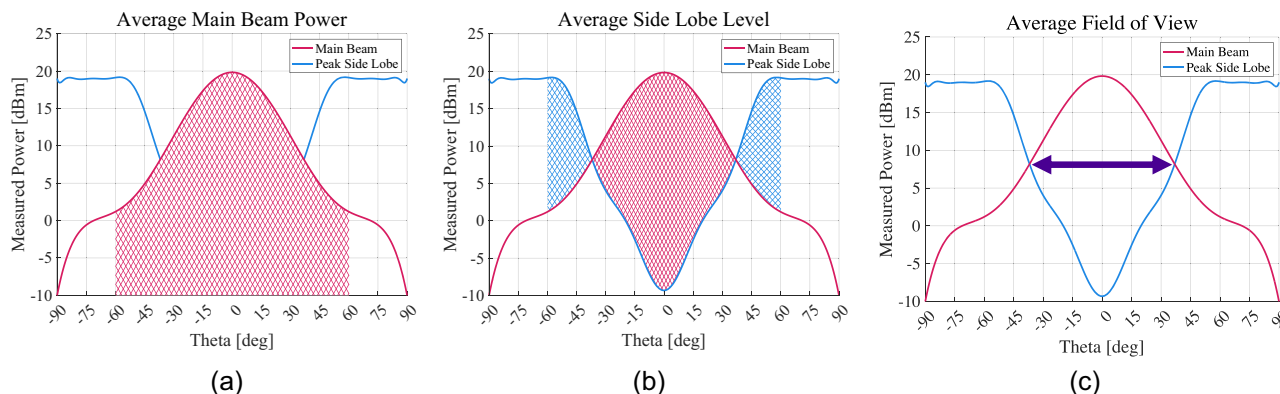
Figure 2. Visualization of optimization criteria. (a) The main beam power is integrated within the theoretical field of view, e.g. ±60°. (b) The difference between the main beam power and peak side lobe power, the side lobe level, is integrated within the theoretical field of view. (c) The field of view optimization maximizes the angular difference between the first crossings of the main beam power and the peak side lobe power.

beam strength is higher within the FoV, the beam on the outside is not truly the main beam, but a grating lobe of the beam on the inside. The FoV of an ideal λ-spaced array is ±30°, greatly reducing the number of measurements.

Array characterization time

An efficient measurement approach is necessary to perform *in-situ* optimization. In a radiation pattern measurement, the average time to move the antenna under test between measurement points, T_{move}, is on the order of seconds, while the measurement time, T_{meas}, can theoretically be less than a microsecond. Assuming $T_{meas} \ll T_{move}$, the time to characterize a phased array is:

$$T_{char} \approx N_b(N_m + 1)T_{move}, \tag{1}$$

where N_m is the number of measurement points per beam and N_b is the number of beams used to characterize the array.

Equation 1 is the fixed time required to move between all the measurement points. If T_{move} is one second, then it takes 90 minutes to characterize *a single meta-gap configuration* along two cuts with 5° precision. If M states are measured sequentially than the total measurement time is MT_{char}.

Instead, multiple configurations can be measured in parallel by iterating through them at each measurement point. Thus a large number of configurations can be characterized while only moving through measurement points once. In this case, the time to characterize a batch of M configurations is:

$$T_{batch} \approx (N_b + N_m)T_{move} \\ + MN_b[N_m + (N_{tiles} - 1)D]T_{meas}, \tag{2}$$

where N_{tiles} is the number of tiles and D is the number of measurements required to optimize the beam phase settings.[2]

For a sufficiently large batch size the total characterization time is decreased by orders of magnitude. However, results are not available until the entire batch is processed. Thus algorithms must operate on batches of measurements, as no decision can be

made until the completion of each batch. The measurement time of this method of sequential batches is simply Equation 2 times the number of batches.

Characterizing the meta-gap optimization problem

Meta-gaps present a high-dimensional configuration space with a far smaller subspace of useful solutions; a meta-gap structure with k switches has 2^k possible states. Finding an optimal state for this kind of switching network has been proven to be NP-Hard in general and there is no known convex heuristic that consistently identifies solutions close to the optimal one [4].

Thus, non-convex heuristic algorithms must be employed in order to identify preferred, if not optimal configurations. While problem-specific heuristics will outperform abstract metaheuristic algorithms [36], it is not obvious how a given set of switches will alter the array behavior due to the strongly nonlinear behavior of switched networks and the complex interactions of parasitic elements in response to different electromagnetic excitations for different steering angles.

Four different metaheuristic algorithms and a simple random search are employed to both explore meta-gap performance and to provide insight into the general structure of the optimization problem and its solutions. The selected algorithms—Genetic Optimization (GEN) [37], variable neighborhood search (VNS) [38], Particle Swarm (PS) [39], and Simulated Annealing (SA) [40]—ake advantage of different properties of the optimization problem [41]. Genetic optimization excels at problems that contain underlying "features" that can be exploited. VNS takes a local to global approach, performing well on problems with clustered optima. SA has the opposite approach, performing a wide area search before settling into a local optima. Like SA, PS takes a global to local approach but incorporates several agents that investigate local optima. Finally, the random search serves as a baseline comparison. Thus, properties of the problem structure can be identified by comparing the relative performance of these methods.

Optimization framework

The same optimization framework is used in both the simulated statistical experiments discussed in Section "Simulated Statistical Analysis" and the *in-situ* optimization experiments discussed in

---

[2]Note that there is an error in Equation (2) of the original paper [35] that underestimates the speed increase.
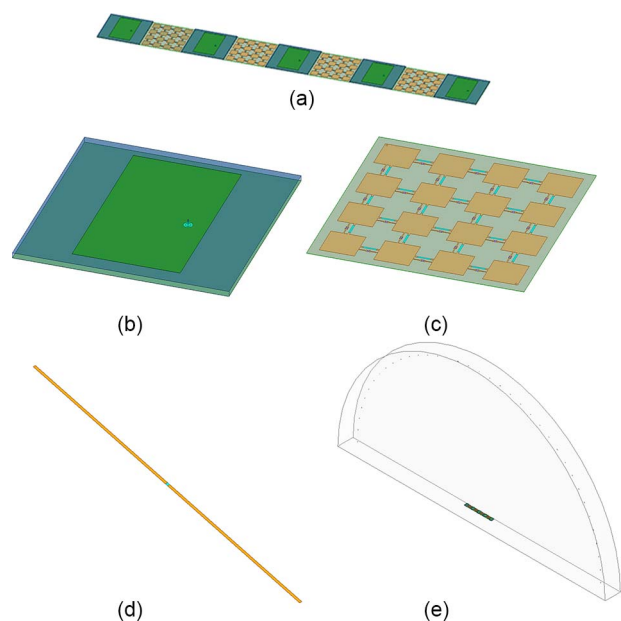
Figure 3. Finite element simulation model. (a) The five element λ-spaced array with embedded meta-gaps. (b) Closeup of antenna model with excitation port. (c) Closeup of meta-gap model with control ports. (d) Closeup of dipole sense antenna. (e) Simulation volume with array and sense antennas in the far-field.

"*In-Situ* Optimization Experiments" section. The metaheuristic algorithm selects switch states to be measured, the measurement range (either real or simulated) measures the desired array characteristic for the selected states, and the results are provided back to the algorithm to select the next states to be measured. After a predefined number of iterations, the algorithm is terminated.

As discussed in "Demonstration Array" section, the demonstration array has 2^{960} different possible meta-gap states. In the simulated experiment and the initial *in-situ* experiment, each meta-gap sheet is constrained to have the same switch settings. The rational for this relatively arbitrary restriction is twofold, first, it restricts the total search space to 2^{24} possible switch settings and, second, the difference in field perturbations between neighboring states is larger and thus easier to measure. These restrictions are relaxed in the later *in-situ* experiments.

Due to the complexity of phased array characterization, states are measured in batches in order to reduce the total measurement time. The algorithms operate in batches of 24 states so that search based approaches, like VNS and SA, can evaluate every neighboring state in a single batch during the identical sheet experiments. The algorithms are iterated for 30 batches, thus exploring a total of 720 states.

To ensure consistency, the same tuning parameters, run lengths, and batch sizes are used in the different experiments. This consistency allows direct comparison of the relative performance of the different algorithms both in different experiments and when optimizing different criteria.

Simulated statistical analysis

Due to the stochastic nature of the employed metaheuristics, they are best characterized by their performance over a large number of trials. Unfortunately, as discussed in Section "Phased-Array

Optimization," the time required to measure a physical array prevents a large number of trials. Instead, the Lavaei–Babakhani method [4] can be used to perform a large number of simulated trials. While deviations in a simulated model might give inaccurate characterization results, they do not fundamentally change the structure of the optimization problem. Thus, metaheuristic algorithms should perform similarly in both simulation and *in-situ*.

The different optimization algorithms are run 1000 times with random initial conditions. Optimization of MBP, SLL, and FoV are treated separately with their own set of runs. The results of the runs are used to calculate the average and standard deviation of the optimal state identified over time. These statistics provide insight into the convergence time of the algorithms, their relative expected performance, and the variance in runs.

Simulation setup

Figure 3 shows the simulation model used for statistical analysis. It is a five element λ-spaced linear array of patch antennas separated by four meta-gap sheets. Both the meta-gap sheets and patch antennas have the same metal patterns and dimensions as their physical equivalent. The meta-gap sheets also model the 30 nH choke inductors in parallel with switches. Figure 3(e) shows the array and the 37 short dipole sensor antennas located in the far-field every 5° in the steering-plane. This model contains 138 ports—5 excitation ports, 37 sensor ports, and 96 control ports—that are represented by teal rectangles. The total simulation volume including the array and sensor ports is $605\pi\lambda^3$.

The array was simulated using HFSS's finite element solver over 15 h using 23 cores and 218 GB of RAM. The 138 port s-parameter model derived from the FEM simulation enables the behavior of different meta-gap settings to be quickly calculated. This calculation method is encapsulated into a "simulated range" enabling the same optimization algorithms to be used for both simulated and measured optimization experiments.

It is important to note that the simulated problem is only a one dimensional array instead of the full two dimensional demonstration array used for the *in-situ* experiments. A simulation of the full 2D array was not possible due to the significantly larger simulation volume required (closer to $7100\pi\lambda^3$) and the larger number of ports (1058).
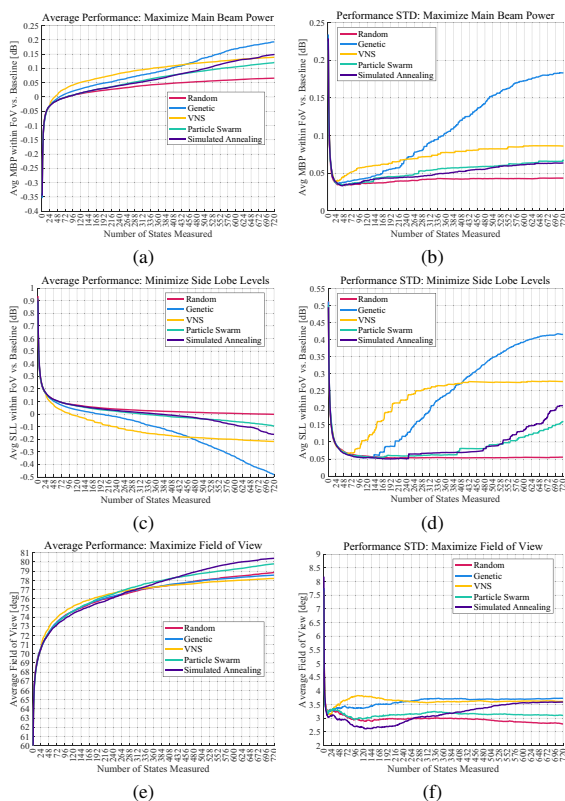
Algorithmic performance

The variable performance of the stochastic algorithms between runs is best described by a probability distribution. Figure 4 compares the average and standard deviations of the algorithms' performance over time for all three optimization criteria. A general summary of the simulated algorithm performance is shown in Table 1.

As can be seen, the algorithms' behavior when maximizing the MBP are similar to their behavior when minimizing the SLL. For both criteria, genetic optimization performs the best on average, but also has the largest standard deviation for performance between runs. VNS converges rapidly on a local optima, but the standard deviation of the performance of that optima is high. The performance of PS and SA is very similar as they both broadly explore the space before converging on a local optima.

The statistical behavior of the algorithms when optimizing the FoV is quite different. For these criteria, PS and SA both perform the best. The most striking result is that both VNS and genetic optimization perform *worse* than the random search. However, the

Table 1. Summary of algorithm performance in simulated experiments.

Algorithm	Random	Genetic	VNS	PS	SA
MBP/SLL performance	Low	High	Medium	Medium	Medium
FoV performance	Low	Low	Very low	High	High
Variability	Low	High	Medium	Medium	Medium
Convergence	Fast	Slow	Fast	Slow	Slow
Dependence on initial conditions	None	High	Very high	Low	None

Figure 4. Comparison of the statistical performance of different algorithms over 1000 trials when (a)–(b) maximizing main beam power, (c)–(d) minimizing side lobe level, and (e)–(f) maximizing the field of view. (a), (c), and (e) show the average performance of the best identified state over time. (b), (d), and (f) show the standard deviation of performance of the best identified state over time.

difference between the average performances is less than 0.5° and so it is possible that the statistical power of the experiment is not large enough for the difference to be statistically significant. Finally, the algorithms have similar standard deviations in performance when optimizing the FoV.

Distribution of states

Because they are randomly selected, the states measured by the random search algorithm provide a statistical sample of the underlying distribution of states. For each of the optimization criteria, the random algorithm explored approximately 705,000 unique states out of 16.8 million over the 1000 runs.

Figure 5 contains histograms of state performance for the different optimization criteria and thus illuminates the underlying distribution of states. The distributions for MBP and SLL are

closely related, with a long tail of states that perform worse than baseline and a sharp drop-off in states that perform better. For MBP optimization, the sample mean and standard deviation are −0.35 and 0.23 dB, respectively, while they are 0.92 and 0.50 dB for SLL optimization. The distribution of states indicates that most meta-gap settings are detrimental to performance, but there a small number of states that offer performance improvements. This aligns with the intuition that random parasitic metal patterns in close proximity to an antenna will generally degrade its pattern and matching.

The histogram for the FoV optimization shown in Figure 5(c) is radically different. The distribution is trimodal, with a sharp thin collection of states close to 60°, the ideal FoV for a λ-spaced array, and two wider loci around 67° and 45°. The high concentration of states indicates that most switch settings do not really affect the FoV. However, there exist sub-spaces that either enhance or suppress the grating lobes to some degree. The sample mean and standard deviation for FoV optimization are 59.7° and 7.8°. This standard deviation is misleading, however, as the variation is mostly attributed to the distinct modes with the center and right modes exhibiting far lower variability.

Demonstration array

Array design

To experimentally test the performance of flexible meta-gaps, they are incorporated into a planar λ-spaced 2D demonstration array. The well-established grating lobe behavior of this structure makes it an ideal test case for examining the behavior of meta-gaps.

The 2.5 GHz array, shown in Figure 6(a), consists of 25 radiating tiles separated by 40 meta-gap sheets. Both the tiles and the sheets are 6 cm squares—$\frac{\lambda}{2}$ at the operating frequency—and are mounted through corner holes to nylon standoffs connected to a rigid wooden backboard. As each sheet contains 24 switches, the total array contains 960 independently programmable switches. In total, the array has 2^{960} different possible meta-gap configurations.

Each tile in the array is a 2.5 GHz radiator with programmable phase and amplitude. The tiles' RF outputs are synchronized by locking to a 78.125 MHz reference. The signal is radiated by a patch antenna on the opposite side of the tile. The patch ground-plane isolates the radiator from the electronics. Figures 6(b) and 6(d) show both sides of the tile and Figure 6(c) shows the measured and FEM-simulated radiation patterns. The simulated antenna efficiency is 84%.

Each tile also serves as a controller for two neighboring meta-gaps using programmable headers. Power, programming, and reference signals are distributed through the array using a single cable. To reduce the total current carried by the cables, power
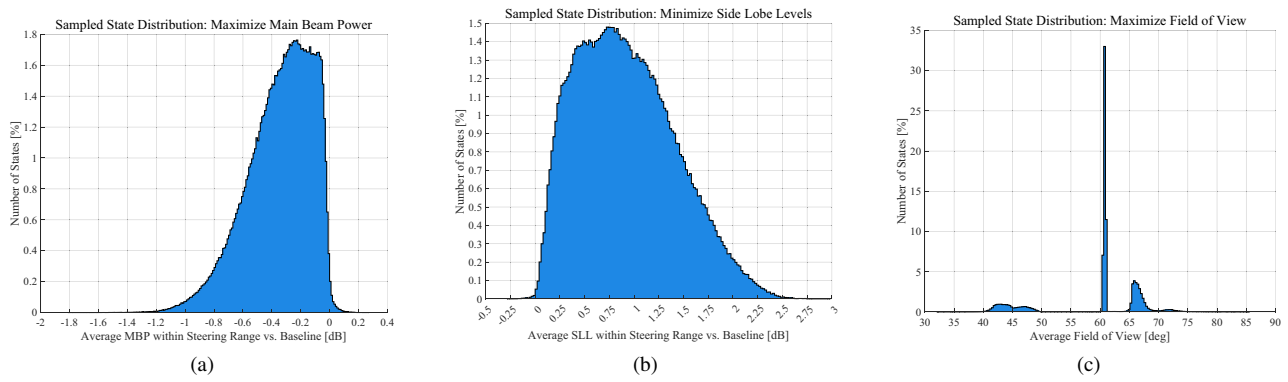
Figure 5. Distribution of the performance of randomly sampled states in the simulation experiment. (a) Main beam power. (b) Side lobe level. (c) Field of view.
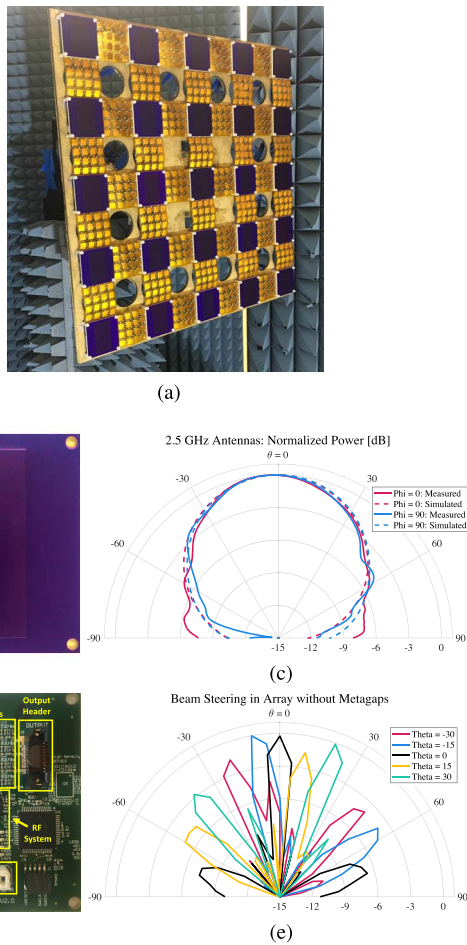

Figure 6. (a) Demonstration array with embedded meta-gaps. (b) Tile antenna. (c) Single tile element pattern. (d) Tile electronics. (e) Measured beam patterns of array without meta-gaps.

is distributed at 30 V and down-converted to 3.3 V by a local DC-to-DC converter on each tile.

Switched meta-gap design

The 6-cm meta-gap sheet shown in Figure 7(a) is comprised of a 0.5-oz copper layer between two 1-mil layers of flexible polyimide. The metal forms a 4-by-4 grid of 9.7mm squares with

5.3 mm gaps. Neighboring squares are connected by an RF switch as shown in Figure 7(b). The metal grid is designed to achieve maximum variation in reflectivity and transparency when all switches are simultaneously turned on and off, respectively. When all the switches are on, the surface ideally behaves like a ground-plane, maximizing the reflection of incident waves. When all the switches are off, the surface ideally is transparent to incident waves. An FEM analysis characterizing the relationship between metal spacing and the surface's ability to reflect incident plane waves is shown in Figure 7(c). A grid spacing of 5.3 mm is selected to minimize the power when the switches are off while reflecting at least 90% of the power when the switches are on. Less than 5.5% of the incident wave power is dissipated by the structure in both the on and off states.

The RF switch, shown in Figure 7(d), consists of a pair of back-to-back PIN diodes biased with a 30 nH RF choke inductor. A common DC ground is established by using 30 nH inductors to connect adjacent squares. PIN diodes are used to maximize the change in switch impedance at RF frequencies and the back-to-back configuration allows an independent DC bias to be established for each switch. The measured switching behavior of the structure is shown in Figure 7(e). At 2.5 GHz, the diode insertion loss is −0.67 dB when on, and the isolation is 15.3 dB when off. Each switch is controlled with a 10 mA current via a header containing 24 control wires and 2 ground wires. The 10 mA bias current optimizes the tradeoff between insertion loss and power consumption. The lightweight 32 AWG wires are connected to the sheet from the back side. The thin substrate and wire configuration maximize sheet flexibility and minimize unwanted near-field interactions.

In-situ optimization experiments

Using an automated test setup, the metahueristic algorithms are used to perform *in-situ* optimization of the demonstration array in a series of experiments. The results of these experiments provide insight into both the realized capabilities of meta-gaps and the underlying optimization problem.

In the initial experiment, each meta-gap sheet is constrained to have the same switch settings in order to restrict the search space. Then, the identical sheet restriction is replaced by different patterns of enforced symmetry in order to explore an increase in the size of the search space and the associated trade-off between the quality of the optimal state and the ability to find it. The best performing symmetry identified in this symmetry experiment, referred to as the E&H near-field mapping, is then used to repeat the evaluation of
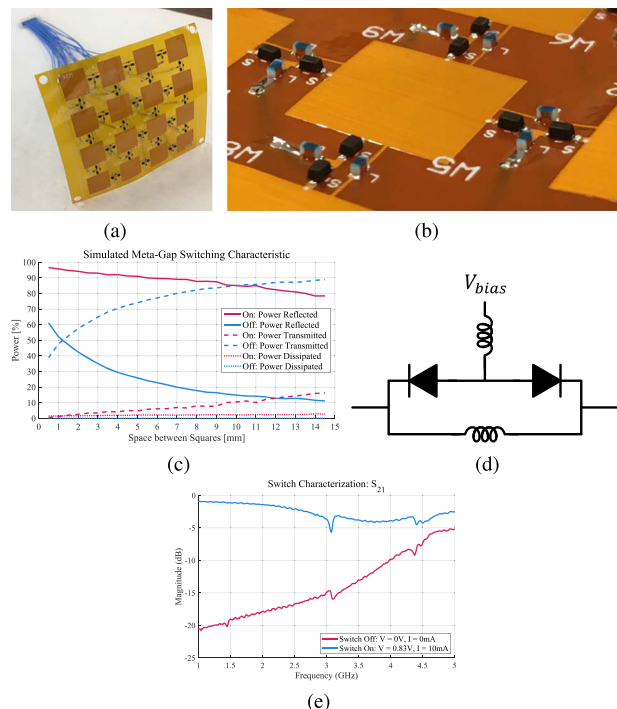
(a)   (b)

(c)   (d)

(e)

Figure 7. (a) Meta-gap sheet. (b) Close-up of switching network. (c) Simulation of reflectivity and transparency versus gap size. (d) RF switch schematic. (e) Measured switch S_{21}.

the optimization criteria and optimization algorithms in the third experiment.

Measurement setup

Figure 8 is a diagram of the automated range measurement system used to perform the *in-situ* optimization. The demonstration array is mounted on a far-field scanner and rotated about the θ and ϕ axes. A frequency generator provides a constant 2.5 GHz signal that is converted to a 78.125 MHz reference using a pair of frequency dividers (total division ratio of 32). This reference is buffered by the array motherboard and distributed through the array under test (AUT). Each tile up-converts the reference back to 2.5 GHz, adjusts its phase, and radiates a fixed power. The combined radiated field is sensed by a horn antenna 2.95 m from the array and is measured by a vector network analyzer set to measure S_{21} at 2.5 GHz. This measured S_{21} is thus a measure of the radiated power relative to a fixed reference.

The host computer runs the metahueristic algorithms and manages the optimization and measurements by programming the array phase and meta-gap settings, controlling the scanner position, and measuring the power from the VNA. The host computer also monitors the array current, radiated spectrum, and temperature throughout the experiment to ensure reliability.

For MBP and SLL optimization, the array is measured by steering beams every 5° from −30° to 30° in the E- and H-plane cuts, while beams are steered every 5° from −90° to 90° for the FoV optimization. Beam steering is achieved by optimizing the tile phases to maximize power in the beam direction. For all criteria, each beam pattern is measured every 5° from −90° to 90° in the E- and H-plane cuts. MBP and SLL optimizations take approximately 23 h while FoV optimizations take 60.
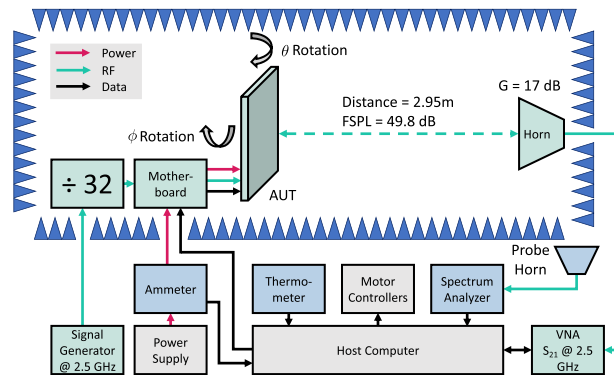

Figure 8. Diagram of measurement setup. Blue triangles indicate RF absorbers and the boundaries of the range. Green components indicate the RF signal path. Grey squares are other critical measurement devices. Blue shapes are auxiliary equipment that monitor the measurement environment.
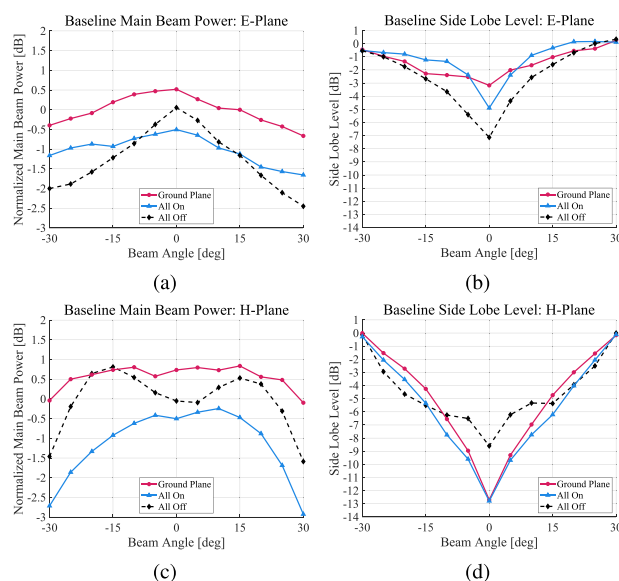

(a)   (b)

(c)   (d)

Figure 9. Baseline measurements of (a), (c) main beam power and (b), (d) side lobe level in E- and H-planes for "all off" state, "all on" state, and ground-plane backed array.

To compensate for low frequency noise and thermal drift over the long measurement periods, each batch measures a reference state, in which every switch is turned off, and uses it to normalize the other patterns. Due to the interwoven nature of the batched measurements, different states in the batch happen in quick succession at a given measurement point; therefore, the difference between these measurements are mostly immune to low-frequency noise and temperature fluctuations. By normalizing each measured pattern to the same reference state, the relative performance of states in different batches can be accurately compared.

Baseline measurements

While useful for measurement purposes, the "all off" state used as a baseline is not indicative of the array performance without the meta-gap sheets. A more appropriate comparison is the relative performance of the meta-gap sheet compared to a simpler approach expected to improve array performance. A reasonable
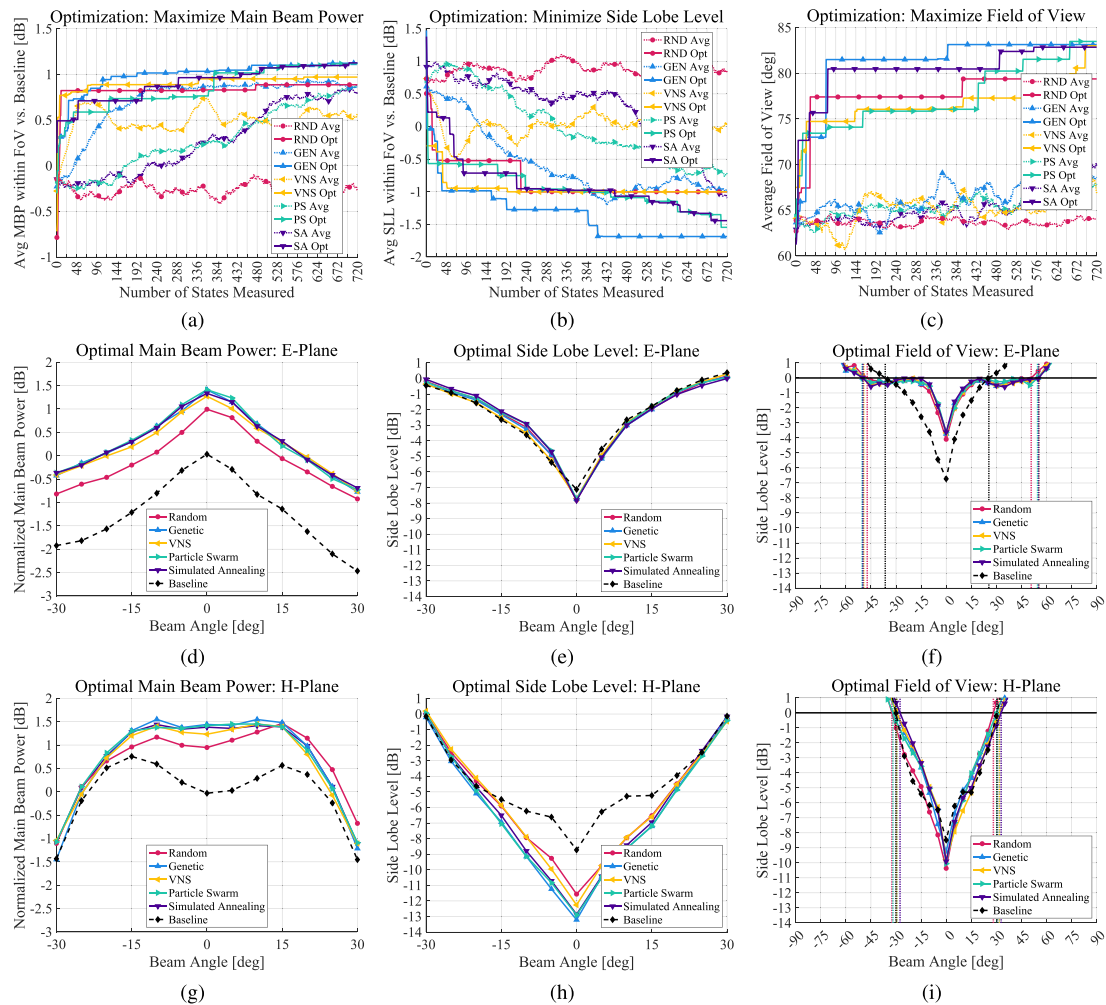
Figure 10. (a)–(c) Optimization curves and (d)–(f) E-plane and (g)–(i) H-plane cuts of the optimal array characteristics for the random search, genetic optimization, VNS, PS, and SA algorithms' optimizations of main beam power, side lobe levels, and FoV under the identical sheet restriction. Optimization plots include the optimal state in addition to the value of the explored states averaged over two batches.

solution is to fill the gaps in the array with a ground-plane, effectively creating a uniform ground-plane commonly found behind elements in an array. However, while a flexible ground-plane would make a superior baseline for comparison, it cannot be rapidly switched to electronically during an experiment.

To enable comparisons between meta-gap performance and a flexible ground-plane, the gaps in the array are filled with a ground-plane comprised of copper tape. By measuring the *absolute* power of the ground-plane backed array and the "all off" meta-gap state, the relative performance can be directly compared. With the relative performance of the "all off" baseline established, the performance of any meta-gap state measured relative to this baseline can be compared to the ground-plane backed array.

Figure 9 shows the MBP and SLL for the ground-plane backed array and meta-gap array in the "all on" and "all off" states normalized by the peak broadside power of the "all off" baseline. The "all on" state is included because it is the meta-gap state that corresponds with a solid ground-plane, even though the "all on" state performs worse than the copper tape ground-plane due to lossy switches and parasitic metals. The average MBP of the "all on" state is 1 dB lower than the ground-plane backed array. In general the ground-plane backed array has higher MBP and lower SLL than

the meta-gap array. The only exception is the E-plane SLL which is lower when the meta-gap array is in the "all off" state.

Identical sheet experiments

In the first set of experiments, each of the five algorithms are used to perform *in-situ* optimization of the MBP, the SLL, and the FoV under the restriction that each meta-gap sheet has the same switch settings. Note that unlike the statistical results in Section "Simulated Statistical Analysis," the presented optimization results are for a *single* run of the experiment. Therefore, caution is warranted when drawing conclusions about the relative performance of the algorithms.

Experimental results are presented in multiple formats. Figures 10(a)–10(c) show both the algorithms' performance over time and a moving average of the performance of states explored over two batches. This average provides another useful view of algorithm behavior. In addition, Figures 10(d)–10(i) shows the optimal array characteristic identified by each algorithm and the "all off" characteristic for each of the three optimization criteria. Finally, an illustration of the best performing meta-gap switch settings for each of the three criteria is shown in Figure 11.

For both MBP and SLL, genetic optimization, PS, and SA have similar final results and outperform both VNS and random search. In both, genetic optimization identifies the best performing state, mirroring the results of the statistical experiments. When optimizing the FoV, all of the algorithms perform similarly, with PS identifying the best state.

The average value of the explored states provides additional insight. While the final MBP and SLL results of genetic optimization, PS, and SA are similar, the genetic optimization's average state value increases much faster initially before leveling off. During this period, the algorithm quickly prunes lower performing genes. SA and PS however converge slower as they explore the full search space. The average performance of states explored by VNS oscillates as the algorithm switches between a focused local search and an unfocused perturbation to escape local optima. In the FoV optimization, however, the performance of the average state explored is similar for each of the algorithms and slowly increases over the course of the run. In all optimization criteria, the stability of the average state explored by the random search indicates long term measurement stability.

Under the identical sheet restriction, meta-gaps are able to increase the average MBP within the FoV by 1.13 dB and decrease the average SLL within the FoV by 1.7 dB when compared to the "all off" baseline. Comparing these improvements to the ground-plane measurements in Section "Baseline Measurements" indicates a 0.23 dB improvement in average MBP and a 2 dB average reduction in SLL compared to the ground-plane backed array. The performance improvement is even higher broadside; meta-gaps increase the MBP by 0.9 dB and a suppress the SLL by 4.6 dB when the beam is steered broadside.

Interestingly, even the random search is capable of suppressing the average SLL 1.3 dB more than the ground-plane backed array and improving the average MBP by at least 0.89 dB compared to the baseline, only 0.01 dB lower than the ground-plane backed antenna. Therefore it is relatively straightforward to identify meta-gap states that perform at least as well as the ground-plane backed array.

Meta-gaps are also able to increase the FoV to 83.5°, 23.5° higher than the theoretical value of a λ spaced array. However, on examining the optimal E-plane SLL characteristic in Figure 10(f), it is clear that the FoV is improved by *increasing* SLL. The SLL is just barely negative for most of the expanded FoV, indicating the main lobe is only slightly higher than the peak side lobe. While this technically meets the definition of FoV, it does not follow the *spirit* of the concept and thus renders the results relatively impractical.[3] Nonetheless, the fact that FoV extension is even possible suggests that meta-gaps can change the aliasing behavior of the array.

Figure 11 shows the optimal meta-gap sheet switch settings for the three optimization criteria. Interestingly, the optimal MBP and SLL states are nearly identical. Both shapes suggest a split "H" shape with vertical symmetry. The optimal FoV state, however, exhibits limited symmetry with no recognizable pattern.

Symmetry experiments

The optimal states identified under the identical sheet restriction are within the larger 960 degree of freedom space and thus

[3]This behavior is not particularly surprising as exploiting the technicalities in the framing of a problem is the modus operandi of optimization algorithms.
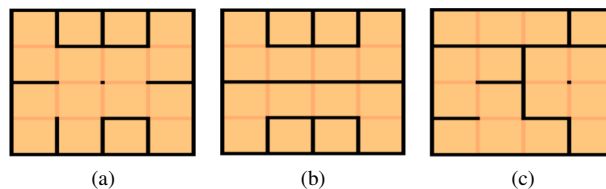

Figure 11. Visualization of optimal solution states for (a) main beam power, (b) side lobe level, and (c) field of view optimizations under the identical sheet restriction. The meta-gap sheet is represented using a four-by-four grid of light copper-colored squares separated by either black, or darker copper-colored lines. These lines indicate the status of each switch in the state; black lines indicate the switch is off while copper colored lines indicate it is on. Thus the shape of the formed conductor pattern can be visualized while still identifying the location of switches.
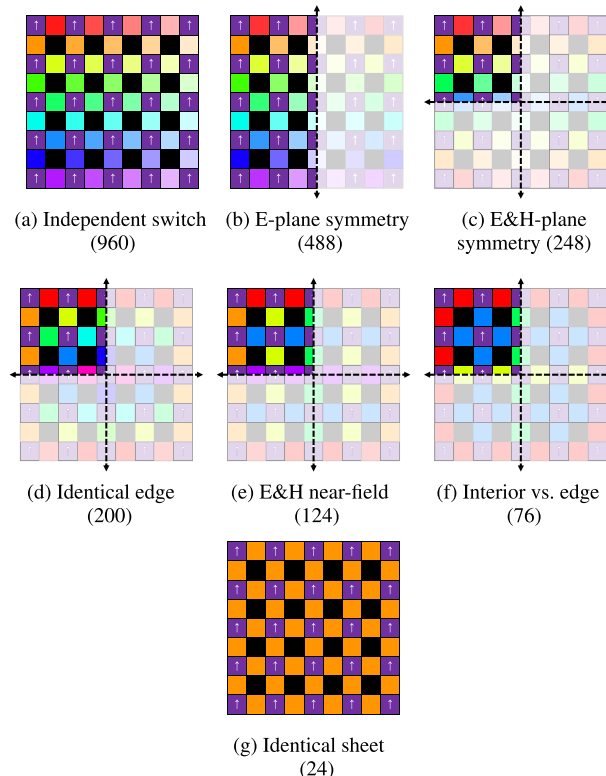

(a) Independent switch (960) (b) E-plane symmetry (488) (c) E&H-plane symmetry (248)

(d) Identical edge (200) (e) E&H near-field (124) (f) Interior vs. edge (76)

(g) Identical sheet (24)

Figure 12. Diagram of mappings used to reduce degrees of freedom. The dark purple squares with arrows indicate the location and polarization of the array antennas. Black squares are the empty gaps between meta-gap sheets. Dashed lines indicate lines of enforced symmetry with mirrored switched settings across the entire array. Sheets with the same color have identical or mirrored switch settings. Each mapping is labeled by the name of the mapping and the number of degrees of freedom.

represent a minimum bound on the unrestricted optimal array performance. Therefore, it is possible to identify further improvements in performance by relaxing this restriction. However, this potential to increase performance comes at the cost of exponentially increasing the search space making it less likely that the algorithms can find the optimal state. Thus, there is a trade-off between the performance of the optimal state and the likelihood of identifying the state.

By considering properties that the optimal solutions are likely to have, it is possible to restrict the search space without eliminating the best performing states. It is likely that the optimal state will be symmetric due to the array symmetry. In addition, it is possible that
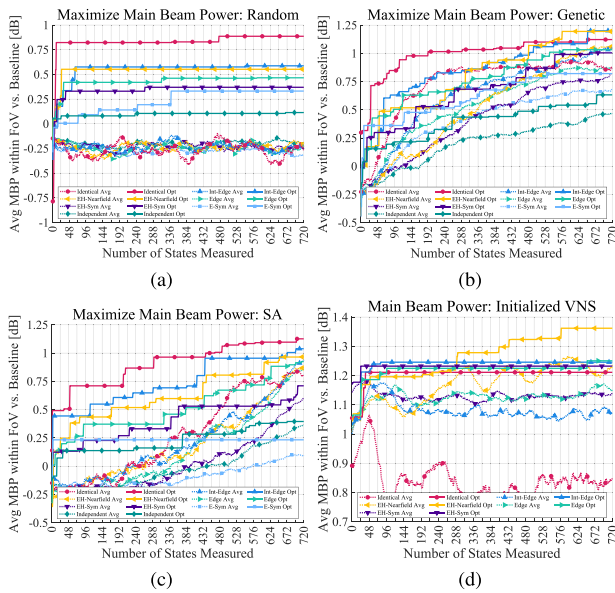
Figure 13. Main beam power optimization curves for (a) random search, (b) genetic optimization, and (c) simulated annealing under different switch mappings. (d) Main beam power optimization curve for variable neighborhood search under different switch mappings when initialized with the best performing state identified in the identical sheet experiments. Plots include the optimal state in addition to the value of the explored states averaged over two batches.

regularity within the E- and H-planes is desirable to create a consistent near-field environment for each antenna. However, it is not clear which combination of enforced symmetries and restrictions must be true for the optimal state.

To explore the impact of different symmetries and restrictions, the MBP is optimized under seven switch mappings with different enforced symmetries and degrees of freedom. Figure 12 includes diagrams of the seven mappings; each diagram is a simplified representation of the array using a grid of squares. The degrees of freedom in each mapping ranges from 24 for the previously explored identical sheet mapping shown in Figure 12(g), to 960 for the completely unrestricted independent switch mapping shown in Figure 12(a). The remaining mappings enforce some combination of horizontal and vertical symmetry, interior sheet vs. edge sheet symmetry, or near-field symmetry. In should be noted that, except for the identical sheet mapping, the more restrictive mappings are sub-spaces of the less restrictive mappings.

Array performance under each mapping is optimized using the SA, genetic optimization, and random search optimization algorithms. Random search is selected to establish a baseline, genetic optimization is selected due to its high performance in the identical sheet experiments, and SA is selected because it has lower variance than genetic optimization, yet still performs well. As another test, the optimal MBP states identified in the identical sheet experiments are used as initial seeds for VNS on the different mappings. By comparing the results of these different experiments, the optimal mapping is identified.

Figure 13 shows the optimization results of these experiments. For the random search, the mappings with more degrees of freedom perform worse than those that are more restricted. This is expected as the performance of the random search increases with the variability of the search space, and restricting the search space increases the electromagnetic variation between randomly selected states.

In the genetic optimization experiment, the identical sheet restriction does not give the best results. Rather, slightly increasing the degrees of freedom with the interior vs. edge mapping and the E&H near-field mapping allows a better state to be identified. In both cases, the average state explored did not converge before the end of the experiment, indicating that a longer experiment might improve performance further. However, larger degrees of freedom degrade performance, with the independent switch mapping performing the worst.

Unlike genetic optimization, none of the mappings used in the SA experiment resulted in a better performing state than the identical sheet restriction. However the general order of the mappings' performance is the same,[4] indicating that the interior vs. edge and E&H near-field mappings are indeed able to identify better solutions than the others.

The initialized VNS experiments demonstrated the same general trend; adding degrees of freedom improves performance initially before it starts to degrade. Due to the clarity of this trend, the E-plane symmetry and independent switch mappings were not explored. As can clearly be seen, the E&H near-field mapping resulted in significantly better performance than any other mapping with a 1.36 dB improvement over the baseline, or 0.46 dB improvement over a ground-plane backed array. The remarkable performance of this mapping suggests that it could be an outlier and that if the optimization was run many more times, on average the performance of this mapping would not be quite as high. However, it is unlikely that the average performance would be substantially worse than this reported result.

An important point of comparison in Figure 13(d) is the performance of the identical sheet mapping. While all of the mappings were *initialized* using the results of the previous identical sheet experiments, this mapping was also *subject* to the identical sheet restriction. This optimization thus serves effectively as an extension of the run-time of the previous identical sheet experiment. Therefore, the greater performances demonstrated by the other mappings over this second identical sheet optimization are likely due to the change in mapping, and not due to the extended run-time of the VNS algorithm.

In totality, the experiments indicate that while additional degrees of freedom can improve performance, at some point the search space is too large to find a high performing state in a reasonable amount of time. Both the interior vs. edge mapping and the E&H near-field mapping strike a balance and result in increased performance. The initialized VNS experiment indicates that the E&H near-field mapping is likely the better performing of the two.

E&H near-field experiments

In the final set of experiments, the E&H near-field mapping is thoroughly explored by optimizing the MBP, the SLL, and the FoV using each of the five optimization algorithms. As with the identical sheet experiments, the algorithms are not initialized in order to emulate the practical scenario where little is known about the array in advance.

Figure 14 shows the algorithm's performance over time in addition to the optimal array characteristic identified by each algorithm. The similarities and differences between the Identical Sheet experiments and the E&H near-field experiments are illuminating.

---

[4]The only exception being a particularly poor performance by the E-plane symmetry mapping.
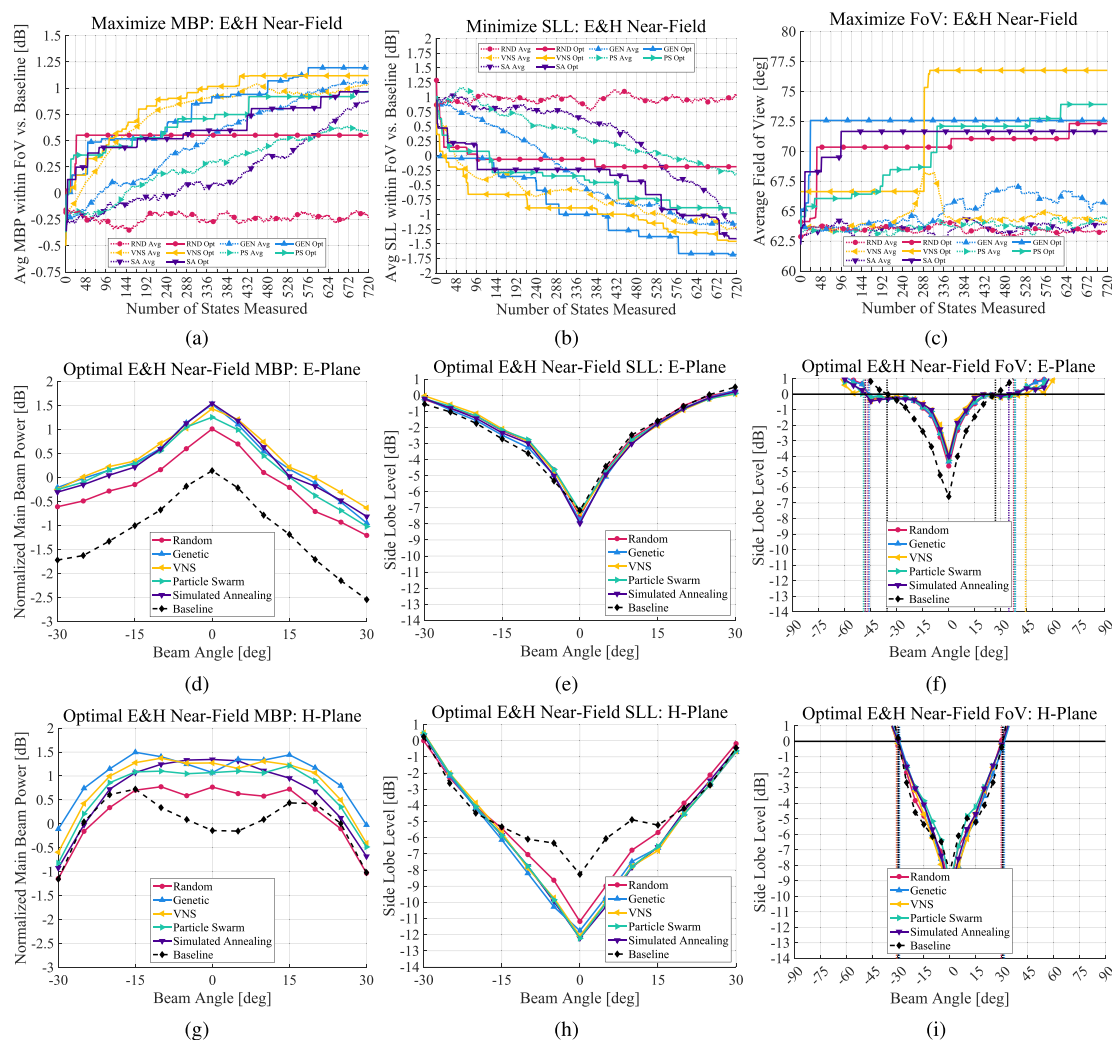
Figure 14. (a)–(c) Optimization curves and (d)–(f) E-plane and (g)–(i) H-plane cuts of the optimal array characteristics for the random search, genetic optimization, variable neighborhood search, particle swarm, and simulated annealing algorithms' optimizations of main beam power, side lobe levels, and field of view under the E&H near-field mapping. Optimization plots include the optimal state in addition to the value of the explored states averaged over two batches.

While genetic optimization still performs the best when optimizing the MBP and SLL, VNS outperforms SA and PS. For FoV optimization, only the VNS is able to make substantial improvements over random search; the other algorithms performed similar to, or even *worse* than the random search. For all of the optimization criteria, the global to local approaches are less successful as the search space increases.

The magnitude of the optimization results indicate that only modest improvements are gained by relaxing the identical sheet restriction. The state that maximizes the average MBP within the FoV increased it by 1.2 dB compared to the "all off" baseline, a 0.07 dB improvement over the identical sheet restriction. This corresponds to a 0.3 dB enhancement compared to the ground-plane backed array. The state that minimizes the average SLL within the FoV suppresses it by 1.7 dB compared to the baseline, the same suppression achieved by the optimal state under the identical sheet restriction. The optimal FoV identified in the E&H near-field mapping, 76.8°, is actually worse that the optimal FoV identified by random search in the identical sheet experiment. Thus, increasing the degrees of freedom strictly resulted in worse performance for FoV optimization. The array characteristics of the

optimal state resemble those of the optimal states under the identical sheet restriction, which is not surprising given their similar performance.

The increased difficulty of the search is demonstrated by the slower convergence rates of both genetic optimization and VNS when optimizing the MBP and SLL. The average values of explored states also converge slower than in the identical sheet experiments. Indeed VNS does not begin to oscillate until over halfway through the run, indicating that it takes a long time to identify a local maxima. These convergence rates and average state performance when optimizing the FoV indicate that each of the algorithms, except VNS, essentially behave like a random search. On the other hand, VNS is able to improve performance as it quickly optimizes a local maxima if it randomly encounters one.

Discussion

Meta-gap performance

The *in-situ* optimization experiments demonstrated that meta-gaps are able to increase the average MBP within the FoV by 0.46 dB

and decrease the average SLL within the FoV by 2 dB, compared to a ground-plane backed array. The FoV can be increased by 23.5° compared to the theoretical 60° FoV for a λ—spaced array. These measured performance improvements represent a *minimum bound* on the possible achievable improvements, as it is unlikely any of the optimal states identified are the true global optima. Given that only around 43,000 of the 2^{960} different states were characterized, it is likely that even greater performance is possible.

However, another conclusion is that finding optimal solutions is difficult due to the vastness of the search space. At some point, additional degrees of freedom reduce the performance of the state that can be found within a limited time-frame. Indeed, the identical sheet restriction produced states with similar performance to those under the E&H near-field mapping despite it being an arbitrary and sub-optimal restriction.

Structure of the optimization problem

The relative performance of the different algorithms within the different experiments gives insight into the underlying optimization problem structure. All of the experiments indicate that the MBP and SLL optimization problems are tightly linked and different than FoV optimization. Thus, it is likely that algorithms or approaches that work well on one of the problems will work well on the other.

In addition, the identical sheet experiments suggest that the MBP/SLL problem has many sparsely-spaced local minima in a relatively gradual global basin. Because VNS quickly identifies a decent solution and then plateaus, it is likely that local minima are relatively shallow and far apart. As the global to local approach of SA and PS are able to make consistent improvements, it is likely that there is some sort of global basin. The existence of this gradual basin is supported by the fact that a random search is able to quickly identify a solution with performance on par with a ground-plane backed array, despite random switch settings degrading performance on average.

However, the most critical observation is that genetic optimization out performs the other algorithms under both the identical sheet restriction and the E&H near-field mapping, suggesting that the MBP/SLL problem solutions are comprised of features with intrinsic value. This matches intuition about the electromagnetic problem as certain patterns of conductors, like closed loops or lines of a specific length, will have a pronounced effect on the electromagnetic fields. The large variance of genetic optimization demonstrated in the simulated experiments is likely caused by which features, if any, are present in the initial batch of elements, as the algorithms do not run long enough for mutation to play a substantial role. The success of genetic optimization suggests that there likely exists a smaller set of basis solutions that could greatly reduce the search space.

Another conclusion is that the FoV optimization problem is quite different; the optimization space is much flatter with most states having little effect and only pockets of minor improvement. This is demonstrated by the very gradual average-state enhancement under the identical sheet restriction and the almost non-existent average-state enhancement in the E&H near-field mapping. In fact, the problem under the E&H near-field mapping does not contain enough global variation for the algorithms to take advantage of, as their convergence behaviors resemble that of random search. Only VNS is able to make improvement because it ascends to a local maxima. In addition, genetic optimization does not offer substantial improvement over the other methods, suggesting that the FoV optimization problem likely does not contain a set of basis solutions.

Possibility of enhanced algorithmic performance

The possible existence of a set of basis states for the MBP/SLL optimization problem shows great promise for reducing the optimization time, and thus enhancing the meta-gap performance. While the binary switching optimization problem is NP-Hard *in general*, particular constraints can reduce the problem complexity, potentially making it convex. If a set basis can be identified, then genetic optimization can become significantly more efficient, as it can be initialized with only the features that are required to produce high-quality solutions. Depending on the properties of the basis set, it could be possible to design the meta-gaps to *only* contain basis states, reducing the number of switches and their parasitic effect on the radiated fields. Finally, just the existence of some sort of basis set suggests that machine learning could be used to efficiently optimize meta-gaps without specifically identifying the exact basis states.

Alternatively, the similarity in the algorithmic behavior in both the simulated and measured experiments suggests that simulation and modeling errors do not drastically change the optimization problem. Therefore it is possible that optimal states could be identified in simulation and then used to initialize the *in-situ* optimization. In this combined approach, a rapid simulated global search would identify regions of good performance and the *in-situ* optimization would find the local optima.

These enhanced optimization techniques could greatly improve optimization time and allow more of the search space to be covered. This in turn would allow higher performing states to be identified, further increasing SLL suppression and MBP enhancement.

Arrays with different element spacings

This work exclusively studies the optimization problem and performance of meta-gaps in a λ-spaced array. Yet, it is important to consider how the optimization problem and performance will change for an array with different element spacing.

While the meta-gap concept is broadly applicable to any element spacing, their impact on the near-field environment depends on the specific array and element design. Therefore, both the optimization problem and the performance of the optimal state will be different.

Metahueristic algorithms will work on any meta-gap array because they are agnostic of the underlying optimization problem. However, it is also likely that the basis states for the MBP/SLL optimization problem are fundamental to the switched meta-gap structure, and not on the particular properties of a λ-spaced array. Therefore, enhanced algorithmic techniques that perform well on a λ-spaced array will likely also perform well on arrays of different spacing.

Further research into the performance of the meta-gaps and their underlying optimization problem in different array designs will be crucial once high-performing meta-gap optimization techniques are developed.

Conclusions

This paper presents the design of a λ-spaced 2D array with programmable meta-gaps between radiators. The platform is used

to explore the ability of meta-gaps to alter the array characteristics. Measurement results demonstrate that meta-gaps can enhance the main beam power, SLL, and FoV of a sparse array. The comparative performance of algorithms in both *in-situ* optimization experiments and simulated statistical experiments suggest that switched passive networks are good candidates for feature based optimization, such as genetic optimization and machine learning. Experimental results also indicate that intelligently restricting the size of the search space is critical for identifying high performing states.

Competing interests. None declared.

References

1. **Elliott Williams D, Dorn C, Pellegrino S and Hajimiri A** (2021) Origami-inspired shape-changing phased array. In *2020 50th European Microwave Conference (EuMC)*. Utrecht, Netherlands, IEEE, 344–347.
2. **Pressley A** (2010) *Elementary Differential Geometry*. London: Springer London.
3. **Fikes AC, Gal-Katziri M, Mizrahi OS, Elliott Williams D and Hajimiri A** (2023) Frontiers in flexible and shape-changing arrays. *IEEE Journal of Microwaves* **3**(1), 349–367.
4. **Lavaei J, Babakhani A, Hajimiri A and Doyle JC** (2011) Solving large-scale hybrid circuit-antenna problems. *IEEE Transactions on Circuits and Systems I: Regular Papers* **58**(2), 374–387.
5. **Sideris C, Hajimiri A, Yang C, Sung-Yueh W, Sammoura F, Lin L and Alon E** (2015) Automated design of a 3d printed waveguide surface coupler. In *2015 IEEE International Symposium on Antennas and Propagation & USNC/URSI National Radio Science Meeting*. Vancouver, BC, Canada, IEEE, 318–319.
6. **Shirazi M, Huang J, Tianjiao L and Gong X** (2018) A switchable-frequency slot-ring antenna element for designing a reconfigurable array. *IEEE Antennas and Wireless Propagation Letters* **17**(2), 229–233.
7. **Fan Y and Rahmat-Samii Y** (2002) A reconfigurable patch antenna using switchable slots for circular polarization diversity. *IEEE Microwave and Wireless Components Letters* **12**(3), 96–98.
8. **Ngamjanyaporn P, Phongcharoenpanich C and Krairiksh M** (2018) A wideband phase-shifterless switched-beam array antenna. In *2018 IEEE-APS Topical Conference on Antennas and Propagation in Wireless Communications (APWC)*. Cartagena, Colombia, IEEE, 1–2.
9. **Semkin V, Ferrero F, Bisognin A, Ala-Laurinaho J, Luxey C, Devillers F and Raisanen A** (2015) Beam switching conformal antenna array for mm-wave communications. In *IEEE Antennas and Wireless Propagation Letters*, 1–1.
10. **Grau Besoli A and De Flaviis F** (2011) A multifunctional reconfigurable pixeled antenna using mems technology on printed circuit board. *IEEE Transactions on Antennas and Propagation* **59**(12), 4413–4424.
11. **Sung YJ, Jang TU and Kim Y-S** (2004) A reconfigurable microstrip antenna for switchable polarization. *IEEE Microwave and Wireless Components Letters* **14**(11), 534–536.
12. **Nikolaou S, Bairavasubramanian R, Lugo C, Carrasquillo I, Thompson DC, Ponchak GE, Papapolymerou J and Tentzeris MM** (2006) Pattern and frequency reconfigurable annular slot antenna using pin diodes. *IEEE Transactions on Antennas and Propagation* **54**(2), 439–448.
13. **Ouyang J** (2011) A circularly polarized switched-beam antenna array. *IEEE Antennas and Wireless Propagation Letters* **10**, 1325–1328.
14. **Chen Y, Zhang L, Yejun H, Wenting L and Wong S-W** (2021) A pattern reconfigurable siw horn antenna realized by pin diode switches.

In *2021 Computing, Communications and IoT Applications (ComComAp)*. Shenzhen, China, IEEE, 112–115.
15. **Anh Nguyen V and Seoong Ook P** (2011) Compact switched and reconfigurable 4-ports beam antenna array for mimo applications. In *2011 IEEE MTT-S International Microwave Workshop Series on Intelligent Radio for Future Personal Terminals*. Daejeon, Korea (South), IEEE, 1–3.
16. **Kamarudin MR, Hall PS, Colombel F and Himdi M** (2007) CPW-fed disc-loaded monopole array antenna with integrated pin diode switches. In *2007 International workshop on Antenna Technology: Small and Smart Antennas Metamaterials and Applications*. Cambridge, UK, IEEE, 396–399.
17. **Zhang S, Huff GH, Feng J and Bernhard JT** (2004) A pattern reconfigurable microstrip parasitic array. *IEEE Transactions on Antennas and Propagation* **52**(10), 2773–2776.
18. **Chen WH, Sun JW, Wang X, Feng ZH, Chen FL, Furuya Y and Kuramoto A**. (2007) A novel planar switched parasitic array antenna with steered conical pattern. *IEEE Transactions on Antennas and Propagation* **55**(6), 1883–1887.
19. **Luo S, Yingsong L, Jiang T and Beiming L** (2019) FSS and meta-material based low mutual coupling mimo antenna array. In *2019 IEEE International Symposium on Antennas and Propagation and USNC-URSI Radio Science Meeting*. Atlanta, GA, USA, IEEE, 725–726.
20. **Yingsong L and Kai Y** (2017) High isolation two-element mimo antenna array based on embedded meta-material cells. In *2017 International Symposium on Antennas and Propagation (ISAP)*. Phuket, Thailand, IEEE, 1–2.
21. **Wenxing L, Liu Y and Yingsong L** (2016) Meta-material based mutual coupling reduction of circularly polarized array. In *2016 IEEE International Symposium on Antennas and Propagation (APSURSI)*. Fajardo, PR, USA, IEEE, 511–512.
22. **Buell K, Mosallaei H and Sarabandi K** (2007) Metamaterial insulator enabled superdirective array. *IEEE Transactions on Antennas and Propagation* **55**(4), 1074–1085.
23. **Mosallaei H and Sarabandi K** (2004) Antenna miniaturization and bandwidth enhancement using a reactive impedance substrate. *IEEE Transactions on Antennas and Propagation* **52**(9), 2403–2414.
24. **Bernard L and Jaeck V** (2013) Investigations on bandwidth enhancement of low cost printed phased array with reactive impedance substrates. In *2013 IEEE International Symposium on Phased Array Systems and Technology*. Waltham, MA, USA, IEEE, 279–284.
25. **Zhu HL, Cheung SW, Liu XH and Yuk TI** (2014) Design of polarization reconfigurable antenna using metasurface. *IEEE Transactions on Antennas and Propagation* **62**(6), 2891–2898.
26. **Bouslama M, Traii M, Gharsallah A and Denidni TA** (2015) Reconfigurable dual-band 3d frequency selective surface unit-cell. In *2015 IEEE International Symposium on Antennas and Propagation & USNC/URSI National Radio Science Meeting*. Vancouver, BC, Canada, IEEE, 1264–1265.
27. **Bouslama M, Traii M, Denidni TA and Gharsallah A** (2016) Beam-switching antenna with a new reconfigurable frequency selective surface. *IEEE Antennas and Wireless Propagation Letters* **15**, 1159–1162.
28. **Babakhani A, Rutledge DB and Hajimiri A** (2008) Transmitter architectures based on near-field direct antenna modulation. *IEEE Journal of Solid-State Circuits* **43**(12), 2674–2692.
29. **Krairiksh M** (2008) Development of a handset adaptive antenna using phased-array of switched-beam elements. In *2008 International Workshop on Antenna Technology: Small Antennas and Novel Metamaterials*. Chiba, Japan, IEEE, 87–90.
30. **Christodoulou CG, Tawk Y, Lane SA and Erwin SR** (2012) Reconfigurable antennas for wireless and space applications. In *Proceedings of the IEEE*. 2250–2261.
31. **Sievenpiper DF, Schaffner JH, Song HJ, Loo RY and Tangonan G** (2003) Two-dimensional beam steering using an electrically tunable impedance surface. *IEEE Transactions on Antennas and Propagation* **51**(10), 2713–2722.
32. **Victor Hum S and Perruisseau-Carrier J** (2014) Reconfigurable reflect arrays and array lenses for dynamic antenna beam control: A review. *IEEE Transactions on Antennas and Propagation* **62**(1), 183–198.

33. **Huang C, Zappone A, Alexandropoulos GC, Debbah M and Yuen C** (2019) Reconfigurable intelligent surfaces for energy efficiency in wireless communication. *IEEE Transactions on Wireless Communications* **18**(8), 4157–4170.

34. **Venkatesh S, Xuyang L, Saeidi H and Sengupta K** (2021) Reconfigurable multifunctional terahertz holographic metasurface using CMOS chip tiling. In *2021 IEEE 19th International Symposium on Antenna Technology and Applied Electromagnetics (ANTEM)*. Winnipeg, MB, Canada, IEEE, 1–3.

35. **Elliott Williams D and Hajimiri A** (2022) Meta-gaps for mechanically reconfigurable phased arrays. In *2022 52nd European Microwave Conference (EuMC)*. Milan, Italy, IEEE.

36. **Wolpert DH and Macready WG** (1997) No free lunch theorems for optimization. *IEEE Transactions on Evolutionary Computation* **1**(4), 67–82.

37. **Bremermann HJ** (1962) Optimization Through Evolution and Recombination. In *Self-Organizing Systems*. Washington, DC: Spartan Books, 93–106.

38. **Mladenović N and Hansen P** (1997) Variable neighborhood search. *Computers & Operations Research* **24**(11), 1097–1100.

39. **Kennedy J and Eberhart R** (1995) Particle swarm optimization. In *Proceedings of ICNN'95—International Conference on Neural Networks*. Perth, WA, Australia, IEEE, 1942–1948.

40. **Kirkpatrick S, Gelatt CD and Vecchi MP** (1983) Optimization by simulated annealing. *Science* **220**(5), 671–680.

41. **Sörensen K** (2015) Metaheuristics-the metaphor exposed. *International Transactions in Operational Research* **22**(1), 3–18.

D. Elliott Williamstyer received the B.S. and M.Eng. degrees in Electrical Engineering and Computer Science from the Massachusetts Institute of Technology (MIT), Cambridge, MA, USA, in 2015 and 2016 respectively, and a Ph.D. degree in electrical engineering from the California Institute of Technology, Pasadena, CA, USA, in 2022. He joined the faculty of Hofstra University in 2022. His research focuses on developing adaptive electromagnetic systems using novel degrees of freedom. His vision is to create devices with enhanced control of electromagnetic fields that can dynamically adapt to changing environments and needs. Dr. Williamstyer was a recipient of the Analog Devices Outstanding Student Designer Award in 2017, won the 2022 EuMC Young Engineer Prize for his work on flexible meta-gaps, and was awarded a 2023 Innovation Teaching Fellow grant at Hofstra University.

Ali Hajimiri is Bren Professor of Electrical Engineering at California Institute of Technology (Caltech), where he is Director of the Microelectronics Laboratory and Co-Director of Space Solar Power Project. Before joining Caltech in 1998, he worked at Philips Semiconductor, Sun Microsystems, and Bell Laboratories. He has authored and coauthored 2 books, several book chapters, and more than 250 refereed journal and conference technical articles. He has been granted more than 160 U.S. patents with many more pending applications. His research interests include high-speed and high-frequency integrated circuits for applications in sensors, photonics, wireless energy transfer, biomedical devices, and communication systems. Prof. Hajimiri is a Fellow of National Academy of Inventors and IEEE. He was selected to the TR35 top innovator's list. He was a Distinguished Lecturer of the IEEE Solid-State and Microwave Societies. He was the recipient of the Microwave Prize, Feynman Prize for Excellence in Teaching, and several other teaching prizes. He has also won several best paper awards in various conferences. He co-founded Axiom Microdevices Inc., whose fully-integrated CMOS PA has shipped around 400,000,000 units, and was acquired by Skyworks Inc. He is a Co-founder of GuRu Wireless Inc.